Supplement of Atmos. Chem. Phys., 21, 4453–4470, 2021
https://doi.org/10.5194/acp-21-4453-2021-supplement

Atmospheric Chemistry and Physics
Open Access
EGU

Supplement of

Measurement report: Ice nucleating abilities of biomass burning, African dust, and sea spray aerosol particles over the Yucatán Peninsula

Fernanda Córdoba et al.

Correspondence to: Luis A. Ladino (luis.ladino@atmosfera.unam.mx)

Supplementary information

Table S1. Summary of a subset of samples (those with the full size range available i.e., from 0.32 μm to 10 μm) taken from Merida and Sisal during 2017 and 2018 to analyze the results presented in this study. MA, BB, and AD refer to marine aerosol, biomass burning, and African dust, respectively. The last two columns indicate if the chemical composition and the size distributions were available parallel to the INP samples. *two samples were collected at different times during the same day.

Aerosol Type	Place	Date	Chemical composition available	Size distribution available
MA	Sisal	24-01-2017 *	Yes	Yes
		24-01-2017 *	Yes	Yes
		25-01-2017	Yes	Yes
		26-01-2017	Yes	Yes
		27-01-2017	Yes	Yes
		28-01-2017	Yes	Yes
		29-01-2017	Yes	Yes
BB	Merida	27-05-2017	No	No
		03-04-2018	Yes	Yes
		05-04-2018	Yes	Yes
		07-04-2018	Yes	Yes
		08-04-2018	Yes	Yes
AD	Sisal	11-07-2018	Yes	Yes
		12-07-2018	Yes	Yes
		13-07-2018	Yes	Yes
		15-07-2018	Yes	Yes
	Merida	11-07-2018	Yes	No
		13-07-2018	Yes	No
		14-07-2018	Yes	Yes
		16-07-2018	No	No

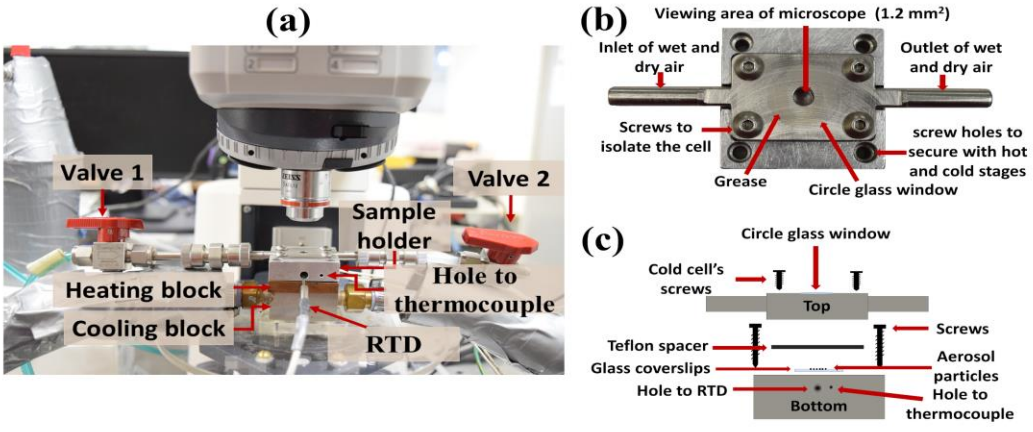

Figure S1. (a) Cold stage showing the sample holder, the heating block, and the cold block (b) a top view of the sample holder, and (c) a schematic diagram of a front view of the sample holder.

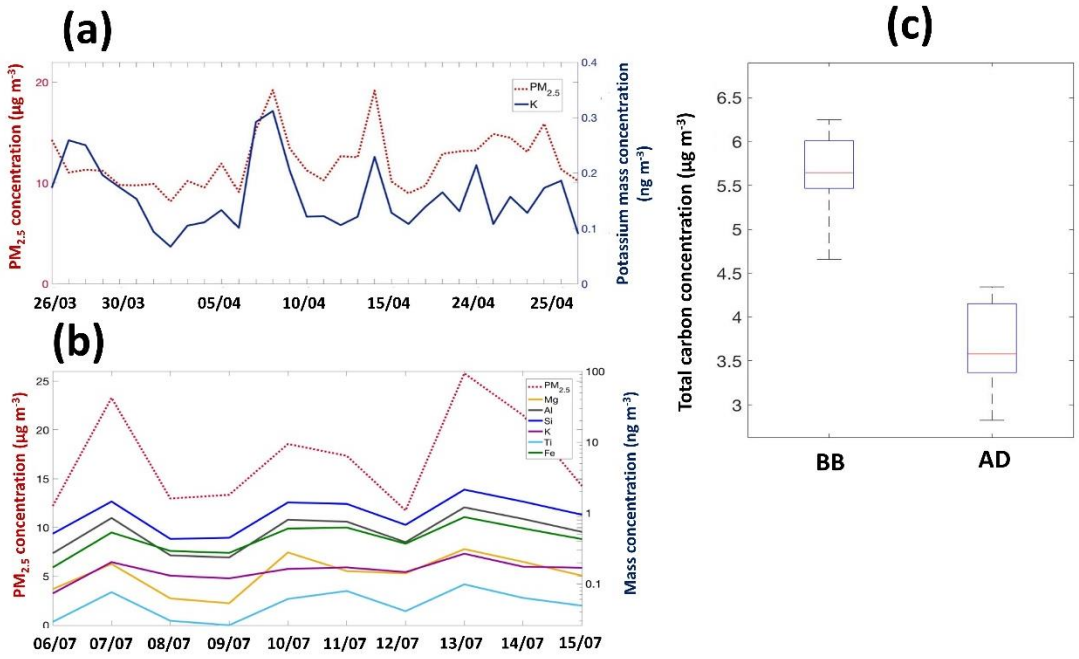

Figure S2. Mass concentration of $PM_{2.5}$ and chemical elements by XRF (a) BB $K_{P.C^*} \geq 0.60$, (b) AD Mg $_{P.C} \geq 0.82$, Al $_{P.C} \geq 0.94$, Si $_{P.C} \geq 0.94$, K $_{P.C} \geq 0.86$, Ti $_{P.C} \geq 0.89$, Fe $_{P.C} \geq 0.88$ and, (c) total carbon concentration for BB and AD. * P.C = Pearson correlation

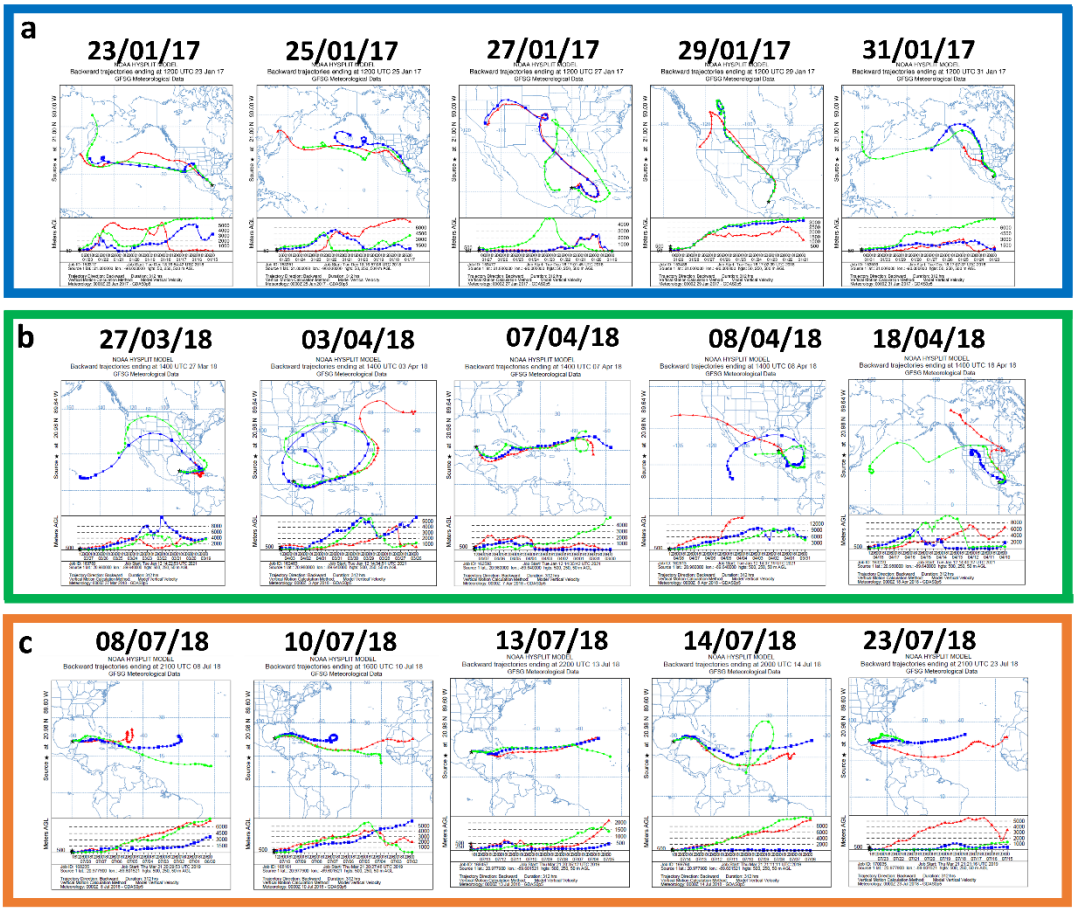

Figure S3. 13-day HYSPLIT back trajectories for the three different air masses for (a) MA-2017, (b) BB-2017, and (c) AD-2018.

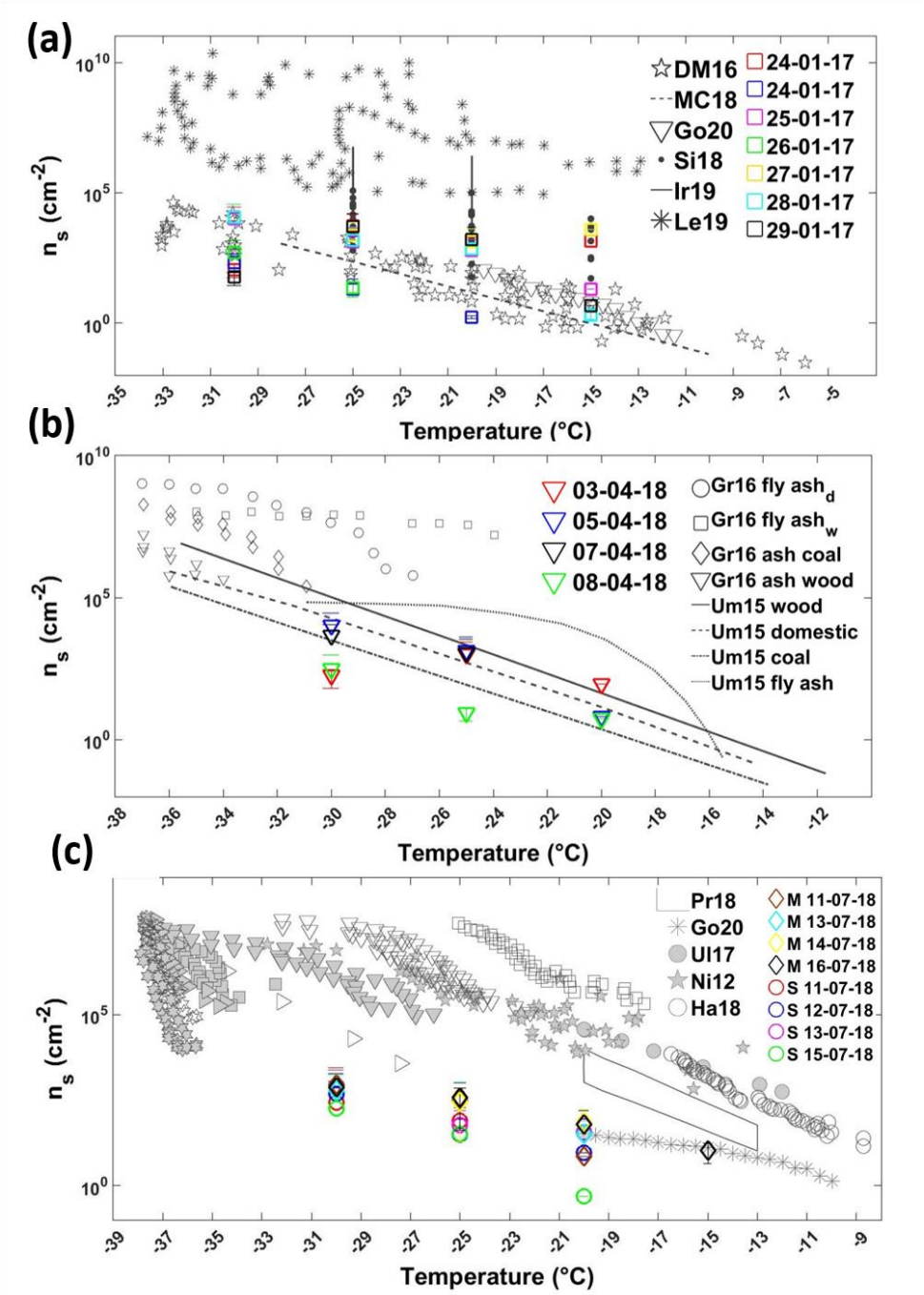

Figure S4. Surface active site density (n_s) as a function of temperature for (a) MA, (b) BB, and (c) AD. Literature data is shown in gray colors. In panel (a), DeMott et al. (2016) (star), McCluskey et al (2018) (dotted line), Gong et al. (2020a) (triangle), Si et al. (2018) (black point), Irish et al. (2019) line, Levin et al. (2019) (asterisk) and the colored squares correspond to the MA samples in this study. In panel (b), Grawe et al. (2016) fly ash dry (circle), fly ash wet (square), ash coal (diamond), and ash wood (triangle), Umo et al. (2015)

wood (solid line), domestic (dashed line), coal (dotdash line) and fly ash (dotted line) and the colored triangles correspond to the BB samples in this study. In panel (c), Price et al. (2018) (rectangle), Gong et al. (2020a) (asterisk), Ullrich et al. (2017) (solid circle), Niemand et al. (2012) (star), Harrison et al. (2018) (open circle), Atkinson et al. (2013) k-feldespar (open square) montmorillonite (solid square), Na/Ca-feldespar (open inverted triangle), quarts (solid inverted triangle), kaolinite (open triangle), chlorite (solid triangle), calcite (open hexagram), mica (solid hexagram), and the colored diamonds and circles to AD samples collected in Merida and Sisal, respectively.

Calculation of surface active site density (n_s)

The methodology employed in this study is based on Si et al. (2018). First, the particle's density was calculated at a given RH ($\rho_{p,RH}$) using Equation S_E1. Later on, *x* factor was calculated following the Equation S_E2. Note that the x factor was computed for each air mass type (MA, AD, and BB). Finally, to obtain the n_s values using Equation S_E3, the particle concentration as a function of their size measured with LasAir and the INP concentrations were necessary. The n_s was obtained for each individual sample listed in Table S1, and therefore, the INP concentration and the particle concentration of each individual sample (and for each period) were used.

a) Calculation of the particle density at a given RH ($\boldsymbol{\rho_{p,RH}}$)

$$\boldsymbol{\rho_{p,RH} = \rho_w + (\rho_{p,dry} - \rho_w)\frac{1}{gf^3}} \qquad \textbf{(S_E1)}$$

where ρ_w is the density of water and $P_{p,dry}$ is the density of the dry particles. 1.87 g cm^{-3} was used for marine aerosol (Si et al., 2018), 2.5 g cm^{-3} for mineral dust particles (Wheeler et al., 2015) and 1.25 g cm^{-3} for biomass burning particles, as it is the average between 1.1 g cm^{-3} and 1.4 g cm^{-3} reported by Li et al. (2016). gf^3 is the hygroscopic growth factor that was obtained from Ming and Russell (2001), using the mean relative humidity for Sisal in January (65%) and July (95%), and for Merida in April (65%) and July (90%). The particles were assumed to be composed of 30% of organic species.

b) Calculation of factor (x).

$$\mathbf{x = gf\sqrt{\frac{\rho_{p,RH}}{\chi\rho_0}}} \qquad (\mathbf{S\_E2})$$

where *x* is the dynamic shape factor for a non-spherical particles and ρ_0 the unit density of 1 g cm^{-3}.

c) Calculation of n_s based on the geometric diameters at a given RH.

$$n_{s\_ae\_RH} = \frac{[INP]}{S_{tot,ae,RH}} = \frac{[INP]}{\pi x^2 D^2_{geo,dry} N_{tot}} \qquad (\mathbf{S\_E3})$$

where *[INPs]* is the concentration of INP (L^{-1}) at each temperature (i.e., -15°C, -20°C, -25°C, and -30°C) for each sample. $S_{tot,ae,RH}$ is the total surface area based on the aerodynamic diameter at the sampling RH, and N_{tot} the total number of aerosol particles. $D_{geo,\ dry}$ corresponds to the average diameter of each LasAir size bin as shown in Table S2. In this case, only the data from channels 1 to 4 from the LasAir were used since these size range overlaps with the MOUDI diameters from stage 2 to 7.

Table S2. LasAir channels and diameters used in the present study with their corresponding surface area.

LasAir channel	Diameter range (μm)	MOUDI stages (μm)	$D_{geo,\ dry}$ (μm)	$D^2_{geo,\ dry}$ (cm^2)
D1	0.3 – 0.5	7 (0.32-0.56)	0.4	1.60×10^{-9}
D2	0.5 – 1.0	6 (0.56-1.00)	0.75	5.62×10^{-9}
D3	1.0 – 5.0	3+4+5 (1.00-5.6)	3.0	8.99×10^{-8}
D4	5.0 – 10	2 (5.6-10.0)	7.5	5.62×10^{-7}

For each sample listed in Table S1, the INP concentration was derived. Also, given that the LasAir continuously measures the particle size distribution (PSD), the total particle concentration (N_{tot}) for each LasAir size bin listed in Table S2 was derived for exactly the same time interval of each INP sample.

As shown in Table S2, the INP concentration from the MOUDI stages 3, 4, and 5 were combined in order that their sizes match those from the LasAir size bins when calculating the n_s values for each sample.

Table S3. Upper and lower limits of the frozen fraction as a function of temperature for five blank experiments (rose shaded area) in Figure 4.

T (°C)	Upper-limit	Lower-limit
0.0	0.00	0.00
-0.5	0.00	0.00
-1.0	0.00	0.00
-1.5	0.00	0.00
2.0	0.00	0.00
-2.5	0.00	0.00
-3.0	0.00	0.00
-3.5	0.00	0.00
-4.0	0.00	0.00
-4.5	0.00	0.00
-5.0	0.00	0.00
-5.5	0.00	0.00
-6.0	0.00	0.00
-6.5	0.00	0.00
-7.0	0.00	0.00
-7.5	0.00	0.00
-8.0	0.00	0.00
-8.5	0.00	0.00
-9.0	0.00	0.00
-9.5	0.00	0.00
-10.0	0.00	0.00
-10.5	0.00	0.00
-11.0	0.00	0.00
-11.5	0.00	0.00
-12.0	0.00	0.00
-12.5	0.00	0.00
-13.0	0.00	0.00
-13.5	0.00	0.00
-14.0	0.00	0.00
-14.5	0.00	0.00
-15.0	0.00	0.00
-15.5	0.00	0.00
-16.0	0.00	0.00
-16.5	0.00	0.00
-17.0	0.00	0.00
-17.5	0.00	0.00

-18.0	0.00	0.00
-18.5	0.00	0.00
-19.0	0.00	0.00
-19.5	0.00	0.00
-20.0	0.00	0.00
-20.5	0.00	0.00
-21.0	0.00	0.00
-21.5	0.00	0.00
-22.0	0.00	0.00
-22.5	0.00	0.00
-23.0	0.00	0.00
-23.5	0.00	0.00
-24.0	0.00	0.00
-24.5	0.00	0.00
-25.0	0.00	0.00
-25.5	0.00	0.00
-26.0	0.00	0.00
-26.5	0.00	0.00
-27.0	0.00	0.00
-27.5	0.00	0.00
-28.0	0.00	0.00
-28.5	0.00	0.00
-29.0	0.00	0.00
-29.5	0.00	0.00
-30.0	0.00	0.00
-30.5	0.00	0.00
-31.0	0.00	0.00
-31.5	0.00	0.00
-32.0	0.00	0.00
-32.5	0.03	-0.01
-33.0	0.03	-0.01
-33.5	0.03	-0.01
-34.0	0.05	0.00
-34.5	0.11	0.00
-35.0	0.35	-0.01
-35.5	0.72	-0.04
-36.0	0.85	0.00
-36.5	1.05	0.22
-37.0	1.10	0.67
-37.5	1.01	0.98
-38.0	1.00	1.00
-38.5	1.00	1.00
-39.0	1.00	1.00
-39.5	1.00	1.00
-40.0	1.00	1.00

Table S4a. Percentage elemental mass concentration for background samples in Merida (second row) and Sisal (third row). Enrichment factors for samples under the influence of BB (fourth row) and AD (fifth row) plumes in Merida as shown in Figure 5.

Elements	Na	Mg	Al	Si	P	S	Cl	K
Merida elemental concentration (%)	30	3	1	7	2	23	13	2
Sisal elemental concentration (%)	17	3	1	2	< 1	12	52	3
Enrichment factor (BB 2018)	0.474	0.786	1.710	0.788	0.308	1.246	0.314	2.413
Enrichment factor (AD 2018)	0.198	1.891	14.771	5.162	0.262	0.905	0.216	2.391

Table S4b.

Elements	Ca	Ti	Cr	Mn	Fe	Ni	Cu	Zn
Merida elemental concentration (%)	5	< 1	3	3	3	< 1	< 1	< 1
Sisal elemental concentration (%)	6	< 1	< 1	< 1	2	< 1	< 1	< 1
Enrichment factor (BB 2018)	0.823	0.604	0.203	0.344	1.819	1.632	0.270	0.560
Enrichment factor (AD 2018)	1.756	3.051	0.156	0.298	5.250	1.749	0.453	0.530

Table S5. Average aerosol size distribution derived from the optical particle counters for the three air masses: marine aerosol (MA), African dust (AD), and biomass burning (BB) as shown in Figure 6.

size range (µm)	Aerosol Particle Concentration (cm^{-3} μm^{-1})					
	MA		**BB**		**AD**	
	MEAN	**STD**	**MEAN**	**STD**	**MEAN**	**STD**
0.3 - 0.5	1.611000	0.923200	5.788500	5.010400	6.302000	1.658000
0.5 - 1.0	0.157200	0.063000	0.119500	0.086000	0.737000	0.096500
1.0 - 5.0	0.007200	0.004249	0.001962	0.000609	0.052720	0.007555
5.0 - 10	0.001825	0.004800	0.000016	0.000002	0.000456	0.000289
10.0 - 25.0	0.000584	0.001500	0.000004	0.000001	0.000012	0.000012

Table S6. INP concentrations (L^{-1}) as a function of temperature (°C) with their corresponding standard deviation as shown in Figure 7a for Marine aerosol (MA), African dust (AD), and biomass burning (BB) particles.

MA											
24/01/2017			24/01/2017			25/01/2017			26/01/2017		
T (°C)	[INP] (L^{-1})	STD	T (°C)	[INP] (L^{-1})	STD	T (°C)	[INP] (L^{-1})	STD	T (°C)	[INP] (L^{-1})	STD
-14	0.292	0.289	-16	0.290	0.286	-5	0.103	0.101	-22	0.386	0.347
-15	0.292	0.289	-17	0.404	0.379	-6	0.103	0.101	-23	0.545	0.452
-16	0.292	0.289	-18	0.472	0.446	-7	0.103	0.101	-24	0.904	0.721
-17	0.629	0.624	-19	0.575	0.549	-8	0.209	0.208	-25	1.258	0.980
-18	0.965	0.957	-20	0.731	0.696	-9	0.283	0.281	-26	2.153	1.506
-19	1.407	1.389	-21	0.778	0.743	-10	0.283	0.281	-27	3.546	2.246
-20	1.674	1.644	-22	0.934	0.900	-11	0.402	0.400	-28	5.763	3.747
-21	2.020	1.990	-23	1.271	1.236	-12	0.402	0.400	-29	7.694	5.109
-22	3.029	2.961	-24	1.796	1.732	-13	0.445	0.443	-30	9.320	6.042
-23	3.797	3.652	-25	4.174	3.535	-14	0.445	0.443	-31	12.684	7.825
-24	6.036	5.705	-26	6.115	4.900	-15	0.491	0.489			
			-27	7.855	6.419	-16	0.590	0.588			
						-17	1.183	1.176			
						-18	1.269	1.262			
						-19	1.724	1.698			
						-20	2.361	2.316			
						-21	2.847	2.780			
						-22	4.303	4.189			
						-23	4.866	4.734			
						-24	6.198	5.941			
						-25	8.940	8.533			
						-26	11.407	10.619			
						-27	13.764	12.840			

Table S6b.

MA								
27/01/2017			28/01/2017			29/01/2017		
T (°C)	[INP] (L^{-1})	STD	T (°C)	[INP] (L^{-1})	STD	T (°C)	[INP] (L^{-1})	STD
-16	0.290	0.286	-15	0.301	0.296	-15	0.068	0.067
-17	0.290	0.286	-16	0.423	0.404	-16	0.468	0.462
-18	0.526	0.520	-17	0.525	0.485	-17	0.653	0.626

-19	0.722	0.713	-18	0.610	0.535	-18	0.973	0.919
-20	0.831	0.787	-19	1.146	1.026	-19	1.302	1.192
-21	0.935	0.891	-20	1.381	1.239	-20	2.110	1.964
-22	1.319	1.207	-21	1.636	1.443	-21	2.568	2.409
-23	1.574	1.460	-22	1.895	1.652	-22	3.883	3.484
-24	1.717	1.594	-23	2.075	1.832	-23	4.069	3.669
-25	1.844	1.674	-24	2.578	2.273	-24	4.969	4.403
-26	2.595	2.215	-25	3.634	3.198	-25	7.491	6.348
-27	3.617	3.008	-26	4.978	4.397	-26	13.119	11.296
-28	4.635	3.802	-27	6.802	5.943	-27	16.797	14.855
-29	6.406	5.276	-28	9.411	8.089	-28	18.895	16.724

135 **Table S6c.**

BB														
27/05/2017			**03/04/2018**			**05/04/2018**			**07/04/2018**			**08/04/2018**		
T (°C)	**[INP] (L^{-1})**	**STD**	**T (°C)**	**[INP] (L^{-1})**	**STD**	**T (°C)**	**[INP] (L^{-1})**	**STD**	**T (°C)**	**[INP] (L^{-1})**	**STD**	**T (°C)**	**[INP] (L^{-1})**	**STD**
-20	0.110	0.108	-19	0.302	0.269	-20	0.063	0.062	-21	0.314	0.309	-20	0.080	0.072
-21	0.530	0.522	-20	0.774	0.636	-21	0.968	0.817	-22	0.460	0.437	-21	0.121	0.113
-22	1.042	0.971				-22	1.478	1.092	-23	1.323	1.050	-22	0.121	0.113
-23	1.749	1.504				-23	2.743	1.853	-24	2.740	2.008	-23	0.265	0.256
-24	2.015	1.661				-24	5.197	3.301	-25	5.283	3.460	-24	0.435	0.423
-25	3.373	2.402				-25	8.660	5.465	-26	7.428	4.795	-25	0.684	0.641
									-27	10.211	6.472	-26	1.153	1.044
												-27	1.735	1.442
												-28	2.682	2.211

Table S6d.

AD											
11/07/2018			**13/07/2018**			**14/07/2018**			**16/07/2018**		
T (°C)	**[INP] (L^{-1})**	**STD**	**T (°C)**	**[INP] (L^{-1})**	**STD**	**T (°C)**	**[INP] (L^{-1})**	**STD**	**T (°C)**	**[INP] (L^{-1})**	**STD**
-19	0.106	0.095	-18	0.071	0.070	-17	0.555	0.361	-9	0.408	0.356
-20	0.228	0.168	-19	0.386	0.380	-18	1.387	0.781	-10	0.408	0.356
-21	0.228	0.168	-20	0.612	0.605	-19	1.735	0.984	-11	0.408	0.356
-22	1.358	1.117	-21	1.384	1.216	-20	3.942	2.398	-12	0.408	0.356
-23	2.641	2.089	-22	3.005	2.630				-13	0.408	0.356

-24	6.814	4.903	-23	6.334	4.999				-14	0.408	0.356
-25	12.718	8.881							-15	0.697	0.488
-26	19.253	13.792							-16	0.839	0.544
-27	36.074	28.630							-17	1.091	0.639
									-18	1.886	1.031
									-19	3.288	1.705
									-20	5.713	2.779
									-21	8.143	4.072

Table S7. Contribution of supermicron and submicron particles to the total INP concentration for Marine aerosol (MA), biomass burning (BB), and African dust (AD) as shown in Figure 7b, c, and d.

	Aerosol Type	**INP > 1 µm (%)**	**INP < 1 µm (%)**
Figure 7b	**MA**	79	21
Figure 7c	**BB**	73	27
Figure 7d	**AD**	72	28

Table S8. Surface active site density (n_s) as a function of temperature for Marine aerosol (MA), biomass burning (BB), and African dust (AD) particles as shown in Figure 8. (-) depicts that data is not available.

	n_s (cm^{-2})					
T (°C)	**MA**		**BB**		**AD**	
	MEAN	**STD**	**MEAN**	**STD**	**MEAN**	**STD**
-30	18080.054	21713.210	12151.720	14874.470	3165.793	1878.310
-25	9778.917	8850.250	4737.786	3352.660	1144.620	976.150
-20	2719.573	2462.670	26.170	44.306	111.968	123.890
-15	773.999	1501.840	-	-	2.725	7.710

Table S9. $PM_{2.5}$ mass concentration (μg m^{-3}) and potassium mass concentration (ng m^{-3}) as shown in Figure S2a.

Date	$PM_{2.5}$ (μg m^{-3})	K (ng m^{-3})
26/03/2018	14.285	0.173
27/03/2018	11.044	0.259
28/03/2018	11.318	0.250
29/03/2018	11.221	0.196
30/03/2018	9.803	0.153
31/03/2018	9.766	0.094
01/04/2018	9.911	0.067
02/04/2018	8.167	0.105
03/04/2018	10.203	0.111
04/04/2018	9.552	0.133
05/04/2018	11.935	0.101
06/04/2018	9.104	0.292
07/04/2018	15.288	0.312
08/04/2018	19.237	0.204
09/04/2018	13.420	0.121
10/04/2018	11.261	0.122
11/04/2018	10.279	0.106
12/04/2018	12.669	0.121
13/04/2018	12.569	0.229
14/04/2018	19.188	0.128
15/04/2018	10.145	0.108
16/04/2018	8.983	0.139
17/04/2018	9.753	0.165
18/04/2018	12.899	0.131
19/04/2018	13.144	0.214
20/04/2018	13.254	0.108
21/04/2018	14.869	0.157
22/04/2018	14.500	0.128
23/04/2018	13.092	0.173
24/04/2018	15.898	0.186
25/04/2018	11.360	0.090

Table S10. $PM_{2.5}$ mass concentration (μg m^{-3}) and mass concentration for different elements (magnesium, aluminum, silicon, potassium, titanium, and iron) as shown in Figure S2b.

Date	$PM_{2.5}$ (μg m^{-3})	Mg (ng m^{-3})	Al (ng m^{-3})	Si (ng m^{-3})	K (ng m^{-3})	Ti (ng m^{-3})	Fe (ng m^{-3})
06/07/2018	12.215	0.084	0.270	0.511	0.073	0.029	0.170
07/07/2018	23.294	0.190	0.850	1.452	0.202	0.076	0.531
08/07/2018	12.977	0.062	0.252	0.431	0.130	0.030	0.291
09/07/2018	13.357	0.053	0.235	0.446	0.119	0.026	0.273
10/07/2018	18.563	0.277	0.803	1.410	0.162	0.061	0.603
11/07/2018	17.348	0.151	0.755	1.345	0.170	0.079	0.623
12/07/2018	11.758	0.140	0.387	0.680	0.146	0.041	0.369

13/07/2018	25.798	0.309	1.202	2.138	0.266	0.098	0.875
14/07/2018	21.497	0.204	0.825	1.448	0.174	0.063	0.607
15/07/2018	14.273	0.130	0.541	0.946	0.168	0.049	0.428

Table S11. Total carbon concentration for the biomass burning (BB) and African dust (AD) periods as shown in Figure S2c.

	BB	**AD**
Mean	5.612	3.899
Standard deviation	0.548	1.028
Median	5.645	3.580
Lower Quartile	5.467	3.357
Upper Quartile 3	6.010	4.153
Lower extreme values	4.658	2.823
Upper extreme values	6.249	6.706
Number of Outliers	0.000	1.000

Table S12. Surface active site density (n_s) as a function of temperature for the Marine aerosol (MA) samples as shown in Figure S4a. (-) depicts that data is not available.

T (°C)	**MA n_s (cm^{-2})**							
	24/01/2017		**24/01/2017**		**25/01/2017**		**26/01/2017**	
	MEAN	**STD**	**MEAN**	**STD**	**MEAN**	**STD**	**MEAN**	**STD**
-15	1426.660	-	-	-	19.440	-	-	-
-20	639.621	1235.103	1.652	0.220	599.926	992.205	-	-
-25	5494.117	9461.367	20.271	26.692	1352.737	3198.148	23.044	13.351
-30	113.313	58.251	210.605	223.945	10263.564	17545.857	520.799	1005.011

Table S12b.

T (°C)	**MA n_s (cm^{-2})**					
	27/01/2017		**28/01/2017**		**29/01/2017**	
	MEAN	**STD**	**MEAN**	**STD**	**MEAN**	**STD**
-15	3961.175	-	2.024	0.628	4.652	-
-20	1355.018	2689.373	717.898	1422.739	1595.946	3157.387
-25	2277.263	5056.142	1487.596	3292.322	4967.164	11014.569
-30	11134.293	22183.018	11656.972	23224.802	56.722	29.508

Table S13. Surface active site density (n_s) as a function of temperature for the biomass burning (BB) samples as shown in Figure S4b. (-) depicts that data is not available.

	BB n_s (cm^{-2})							
	03/04/2018		05/04/2018		07/04/2018		08/04/2018	
T (°C)	MEAN	STD	MEAN	STD	MEAN	STD	MEAN	STD
-15	-	-	-	-	-	-	-	-
-20	92.489	-	6.566	-	-	-	5.632	-
-25	1019.910	1792.072	1324.826	2919.094	1171.566	2342.905	8.962	4.428
-30	184.073	118.441	10782.461	18240.222	4778.386	6795.108	311.240	633.716

Table S14. Surface active site density (n_s) as a function of temperature for the African dust (AD) samples as shown in Figure S4c. (-) depicts that data is not available.

T (°C)	AD n_s (cm^{-2})							
	M 11/07/2018		M 13/07/2018		M 14/07/2018		M 16/07/2018	
	MEAN	STD	MEAN	STD	MEAN	STD	MEAN	STD
-15	-	-	-	-	-	-	10.901	6.502
-20	7.141	-	32.598	48.229	72.157	98.420	62.606	92.129
-25	308.329	674.000	378.340	664.009	285.210	266.140	385.538	344.055
-30	924.082	1889.646	601.991	1130.049	764.985	1138.794	744.400	1136.410

Table S14b.

T (°C)	AD n_s (cm^{-2})							
	S 11/07/2018		S 12/07/2019		S 13/07/2020		S 15/07/2021	
	MEAN	STD	MEAN	STD	MEAN	STD	MEAN	STD
-15	-	-	-	-	-	-	-	-
-20	35.868	54.051	9.196	-	35.936	49.915	0.487	-
-25	78.543	112.902	31.178	54.788	59.759	95.040	33.472	60.238
-30	265.345	461.054	476.947	619.422	814.799	1561.430	182.460	275.026

References

Atkinson, J. D., Murray, B. J., Woodhouse, M. T., Whale, T. F., Baustian, K. J., Carslaw, K. S., Dobbie, S., O'Sullivan, D. and Malkin, T. L.: The importance of feldspar for ice nucleation by mineral dust in mixed-phase clouds, Nature, 498(7454), 355–358, doi:10.1038/nature12278, 2013.

DeMott, P. J., Hill, T. C. J., McCluskey, C. S., Prather, K. A., Collins, D. B., Sullivan, R. C.,

Ruppel, M. J., Mason, R. H., Irish, V. E., Lee, T., Hwang, C. Y., Rhee, T. S., Snider, J. R., McMeeking, G. R., Dhaniyala, S., Lewis, E. R., Wentzell, J. J. B., Abbatt, J., Lee, C., Sultana, C. M., Ault, A. P., Axson, J. L., Martinez, M. D., Venero, I., Santos-Figueroa, G., Stokes, M. D., Deane, G. B., Mayol-Bracero, O. L., Grassian, V. H., Bertram, T. H., Bertram, A. K., Moffett, B. F. and Franc, G. D.: Sea spray aerosol as a unique source of ice nucleating particles, Proc. Natl. Acad. Sci. U. S. A., 113(21), 5797–5803, doi:10.1073/pnas.1514034112, 2016.

Gong, X., Wex, H., Pinxteren, M., Triesch, N., Wadinga Fomba, K., Lubitz, J., Stolle, C., Weinhold, K., Brandy, T., Müller, T., Herrmann, H. and Stratmann, F.: Characterization of aerosol particles at Cabo Verde close to sea level and at the cloud level – Part 2: Ice-nucleating particles in air, cloud and seawater, Atmos. Chem. Phys., 20(3), 1451–1468, doi:10.5194/acp-20-1431-2020, 2020.

Grawe, S., Augustin-Bauditz, S., Hartmann, S., Hellner, L., Pettersson, J. B. C., Prager, A., Stratmann, F. and Wex, H.: The immersion freezing behavior of ash particles from wood and brown coal burning, Atmos. Chem. Phys., 16(21), 13911–13928, doi:10.5194/acp-16-13911-2016, 2016.

Harrison, A. D., Whale, T. F., Rutledge, R., Lamb, S., Tarn, M. D., Porter, G. C. E., Adams, M. P., McQuaid, J. B., Morris, G. J. and Murray, B. J.: An instrument for quantifying heterogeneous ice nucleation in multiwell plates using infrared emissions to detect freezing, Atmos. Meas. Tech., 11(10), 5629–5641, doi:10.5194/amt-11-5629-2018, 2018.

Irish, V. E., Hanna, S. J., Willis, M. D., China, S., Thomas, J. L., Wentzell, J. J. B., Cirisan, A., Si, M., Leaitch, W. R., Murphy, J. G., Abbatt, J. P. D., Laskin, A., Girard, E. and Bertram, A. K.: Ice nucleating particles in the marine boundary layer in the Canadian Arctic during summer 2014, Atmos. Chem. Phys., 19(2), 1027–1039, doi:10.5194/acp-19-1027-2019, 2019.

Levin, E. J. T., DeMott, P. J., Suski, K. J., Boose, Y., Hill, T. C. J., McCluskey, C. S., Schill, G. P., Rocci, K., Al-Mashat, H., Kristensen, L. J., Cornwell, G., Prather, K., Tomlinson, J., Mei, F., Hubbe, J., Pekour, M., Sullivan, R., Leung, L. R. and Kreidenweis, S. M.: Characteristics of Ice Nucleating Particles in and Around California Winter Storms, J. Geophys. Res. Atmos., 124(21), 11530–11551, doi:10.1029/2019JD030831, 2019..

Li, C., Hu, Y., Chen, J., Ma, Z., Ye, X., Yang, X., Wang, L., Wang, X. and Mellouki, A.: Physiochemical properties of carbonaceous aerosol from agricultural residue burning: Density, volatility, and hygroscopicity, Atmos. Environ., 140, 94–105, doi:10.1016/j.atmosenv.2016.05.052, 2016.

McCluskey, C. S., Hill, T. C. J., Humphries, R. S., Rauker, A. M., Moreau, S., Strutton, P. G., Chambers, S. D., Williams, A. G., McRobert, I., Ward, J., Keywood, M. D., Harnwell, J., Ponsonby, W., Loh, Z. M., Krummel, P. B., Protat, A., Kreidenweis, S. M. and DeMott, P. J.: Observations of Ice Nucleating Particles Over Southern Ocean Waters, Geophys. Res. Lett., 45(21), 11,989-11,997, doi:10.1029/2018GL079981, 2018.

Ming, Y., Russell, L.M. Predicted hygroscopic growth of sea salt aerosol. J. Geophys. Res.

Atmos. 106, 28259–28274. https://doi.org/10.1029/2001JD000454, 2001.

Niemand, M., Möhler, O., Vogel, B., Vogel, H., Hoose, C., Connolly, P., Klein, H., Bingemer, H., DeMott, P., Skrotzki, J. and Leisner, T.: A Particle-Surface-Area-Based Parameterization of Immersion Freezing on Desert Dust Particles, J. Atmos. Sci., 69(10), 3077–3092, doi:10.1175/JAS-D-11-0249.1, 2012.

Price, H. C., Baustian, K. J., McQuaid, J. B., Blyth, A., Bower, K. N., Choularton, T., Cotton, R. J., Cui, Z., Field, P. R., Gallagher, M., Hawker, R., Merrington, A., Miltenberger, A., Neely, R. R., Parker, S. T., Rosenberg, P. D., Taylor, J. W., Trembath, J., Vergara-Temprado, J., Whale, T. F., Wilson, T. W., Young, G. and Murray, B. J.: Atmospheric Ice-Nucleating Particles in the Dusty Tropical Atlantic, J. Geophys. Res. Atmos., 123(4), 2175–2193, doi:10.1002/2017JD027560, 2018.

Si, M., Irish, V.E., Mason, R.H., Vergara-Temprado, J., Hanna, S.J., Ladino, L.A., Yakobi-Hancock, J.D., Schiller, C.L., Wentzell, J.J.B., Abbatt, J.P.D., Carslaw, K.S., Murray, B.J., Bertram, A.K. Ice-nucleating ability of aerosol particles and possible sources at three coastal marine sites. Atmos. Chem. Phys. 18, 15669–15685. https://doi.org/10.5194/acp-18-15669-2018, 2018.

Ullrich, R., Hoose, C., Möhler, O., Niemand, M., Wagner, R., Höhler, K., Hiranuma, N., Saathoff, H. and Leisner, T.: A new ice nucleation active site parameterization for desert dust and soot, J. Atmos. Sci., 74(3), 699–717, doi:10.1175/JAS-D-16-0074.1, 2017.

Umo, N. S., Murray, B. J., Baeza-Romero, M. T., Jones, J. M., Lea-Langton, A. R., Malkin, T. L., O'Sullivan, D., Neve, L., Plane, J. M. C. and Williams, A.: Ice nucleation by combustion ash particles at conditions relevant to mixed-phase clouds, Atmos. Chem. Phys., 15(9), 5195–5210, doi:10.5194/acp-15-5195-2015, 2015.

Wheeler, M.J., Mason, R.H., Steunenberg, K., Wagstaff, M., Chou, C., Bertram, A.K.. Immersion freezing of supermicron mineral dust particles: Freezing results, testing different schemes for describing ice nucleation, and ice nucleation active site densities. J. Phys. Chem. A 119, 4358–4372. https://doi.org/10.1021/jp507875q, 2015.